JOURNAL OF GEOPHYSICAL RESEARCH, VOL. 96, NO. B10, PAGES 16,509–16,524, SEPTEMBER 10, 1991

# Surface Deformation and Energy Release Rates for Constant Stress Drop Slip Zones in an Elastic Half-Space

M. WU, J. W. RUDNICKI, C. H. KUO, AND L. M. KEER

*Department of Civil Engineering, Northwestern University, Evanston, Illinois*

Free surface displacements, stress intensity factors, and energy release rates are calculated for planar slip zones in an elastic half-space subjected to a prescribed shear stress drop. Although the method can treat arbitrarily shaped planar zones and distributed stress drops, for simplicity, results are presented only for circular and elliptic zones and uniform stress drops. Calculations of the stress intensity factors and energy release rates for various geometries indicate that solutions for the half-space differ by less than 10% from those in the full space if the distance from the slip zone center to the free surface is greater than the downdip width of the slip zone. In addition, the influence of the free surface is greater for decreasing dip angle. For slip zones that are near the free surface and, especially, those that break the surface there is a coupling between slip and normal relative displacement. That is, for a prescribed shear stress drop and zero normal stress change, slip induces relative normal displacement. As example applications, these solutions are used to reexamine the coseismic geodetic data from three earthquakes: 1966 Parkfield, 1983 Borah Peak, and 1987 Whittier Narrows. The geometries, moments, and stress drops are similar to those inferred in previous studies using dislocation methods. However, the stress drop inferred here may be more reliable because stress drop is one of the parameters adjusted to fit the observed surface deformations. In addition, the method makes it possible to estimate the critical energy release rate at the termination of rupture. Values for the Parkfield, Borah Peak, and Whittier Narrows earthquakes are $1.5 \times 10^6$ J/m$^2$, $1.2 \times 10^6$ J/m$^2$, and $2 \times 10^8$ J/m$^2$, respectively.

## INTRODUCTION

Why do earthquake ruptures start and stop? In order to address this question we require a criterion for propagation. Although rupture criteria in the Earth's crust are not known with any certainty, a simple one that is widely used in fracture mechanics and is often adopted in faulting problems is that the energy released per unit area of slip advance is equal to a critical value [*Rudnicki*, 1980; *Rice*, 1980, 1983; *Li*, 1987]. This criterion is undoubtedly too simple to describe in detail the actual processes of rupture and slip propagation. Nevertheless, when these more complex processes occur in a zone near the fault rupture edge having a length scale much smaller than other relevant lengths, e.g., fault rupture length, distance to the free surface, etc., it is well known that the energy release criterion provides a good description of rupture [e.g., *Rudnicki*, 1980; Rice, 1980, 1983]. Furthermore, because the stress and displacement fields near the edge of a crack in a linear elastic body have a universal form characterized by the stress intensity factors (coefficients of the singular stresses), the energy release rate can be expressed in terms of these factors [*Rice*, 1968].

An impediment to the application of this criterion to slip in the Earth's crust has been the difficulty of calculating stress intensity factors for realistic geometries. Although many results are known for two-dimensional problems and for simple crack shapes in three-dimensional bodies [*Murakami*, 1987], there are few analytical results for cracks in an elastic half-space.

In this paper we present a numerical method for calculating the stresses and displacements in an elastic half-space due to embedded and surface-breaking zones of prescribed stress drop. For simplicity, we present results only for elliptical zones and constant stress drops, but the method is sufficiently general to treat arbitrary planar shapes and spatially varying stress drops. Because the method incorporates the exact asymptotic form of the slip near the edge of a crack in a linear elastic body, results for the stress intensity factors are accurate. Furthermore, the method is based upon integration of the exact form of the displacement due to a point force in a half-space and hence can treat accurately cases in which the slip zone intersects the surface of the half-space.

We present results for the effect of the free surface on the stress intensity factors, the moment, and the energy release rate. Two features are of particular interest: the distance from the free surface at which its effect is negligible and the effect of proximity of the free surface on the tendency of the rupture to propagate toward it.

As applications of this method, we reexamine the coseismic geodetic data for three earthquakes: 1966 Parkfield, 1983 Borah Peak, and 1987 Whittier Narrows. In this approach, the stress drop is a parameter of the model and hence is constrained by comparison of the calculated and observed surface displacements. Furthermore, if the slip zone is assumed to propagate according to the criterion that the energy release rate equals a critical value, then we are able to estimate the critical value at the termination of rupture.

The stress drop method which we use here can be contrasted with the more common dislocation approach. The dislocation approach models slip zones by approximating them as surfaces of prescribed displacement discontinuity. Comparison of the calculated surface deformations with observations is used to infer the geometry of the slip zones and the distribution of slip. An advantage of the dislocation approach is its simplicity: once the solution for an elemental point slip is determined, results for general distributions of slip and complex shapes can be obtained by quadrature. As a result, this approach has become a staple for inferring



Paper number 91JB01043.
0148-0227/91/91JB-01043$05.00

information about slip from surface deformation measurements.

A disadvantage of this dislocation approach is that it is purely kinematic: it relates surface deformation to slip at depth but does not directly yield information about the stresses that produced the slip. More specifically, when the distribution of slip is approximated by constant slip elements (as is usually the case), the average stress change is unbounded. Consequently, stress drop can be inferred only indirectly. For example, the typical method is to calculate the moment and infer the stress drop by using the relation between the moment and the stress drop for a circular crack in an infinite body. Thus the stress drop is determined from a slip distribution that is different from the one inferred from the observations and used to calculate the moment. Furthermore, because the stress near the edge of a zone modeled by constant slip elements is not only singular but nonintegrable, it is not possible to calculate an energy release rate. As a result, the information concerning rupture propagation obtained by this method is limited.

The next section of the paper briefly describes the formulation of the problem and the numerical method used. Succeeding sections present results for the effect of the free surface on slip zones of various geometries and depths and for application of the stress drop approach to reexamine the coseismic geodetic data for three earthquakes.

## METHOD OF ANALYSIS

The goal is to obtain the stress and displacement fields in an elastic half-space caused by a prescribed stress drop on a planar surface of discontinuity $S$. To do this, we develop first an expression for the stress in the half-space due to a prescribed displacement discontinuity. When this expression is evaluated on the surface of discontinuity $S$, it becomes an integral equation for the unknown distribution of displacement discontinuities arising from the prescribed stress change on $S$. This equation is solved by using a numerical method that expresses it as a system of linear algebraic equations. Once the appropriate distribution of displacement discontinuities is determined, other quantities of interest, such as the free surface displacement and the stress intensity factors, can be determined.

Consider an elastic body in which the stresses $\sigma_{ij}$ are related to the displacement gradients $u_{k,l}(=\partial u_k/\partial x_l)$ by

$$\sigma_{ij} = C_{ijkl}u_{k,l} \tag{1}$$

where $C_{ijkl}$ is the tensor of elastic moduli. For the case of an isotropic material considered here $C_{ijkl}$ has the following form:

$$C_{ijkl} = \frac{2\mu\nu}{(1-2\nu)}\delta_{ij}\delta_{kl} + \mu(\delta_{ik}\delta_{jl} + \delta_{il}\delta_{jk}) \tag{2}$$

where $\mu$ is the shear modulus, $\nu$ is Poisson's ratio, and $\delta_{ij}$ is the Kronecker delta. Let $B_1(\xi)$ be relative displacements

$$B_i(\xi) = u_i^+ - u_i^- \tag{3}$$

on a planar surface of discontinuity $S$ with a unit normal $\mathbf{n}$ directed from the (−) to the (+) side of $S$. The resulting displacements elsewhere in the body are given by [e.g., *Steketee*, 1958]

$$u_i(\mathbf{x}) = \int_S C_{klmn}n_m B_n(\xi)\frac{\partial G_{ik}}{\partial \xi_l}(\mathbf{x}, \xi)\, d\xi \tag{4}$$

where $G_{ij}(\mathbf{x}, \xi)$ is the displacement in the $i$th direction at $\mathbf{x}$ due to a unit point force in the $j$th direction at $\xi$. The corresponding stresses are obtained by substituting (4) into (1):

$$\sigma_{ij} = C_{ijkl}C_{pqmn}\int_S n_m B_n(\xi)\frac{\partial^2 G_{kp}}{\partial x_l\, \partial \xi_q}(\mathbf{x}, \xi)\, d\xi \tag{5}$$

Although the displacement discontinuity is unknown, we require that it produce a prescribed stress (drop) $p_j$ on $S$:

$$n_i\sigma_{ij} = -p_j \qquad \text{for } \mathbf{x} \text{ on } S \tag{6}$$

Substitution of (5) into (6) yields the following integral equation:

$$\int_S K_{mn}(\mathbf{x}, \xi)B_n(\xi)\, d\xi = -p_m(\mathbf{x}) \qquad \text{for } \mathbf{x} \text{ on } S \tag{7}$$

where

$$K_{mn} = n_i C_{imkl}C_{pqrn}n_r\frac{\partial^2 G_{kp}}{\partial x_l\, \partial \xi_q} \tag{8}$$

Once the $B_n(\xi)$ are determined from (7), the displacements of any point in the half-space and, in particular, of the free surface can be obtained from (4).

In order to implement these results for elliptical slip zones in a half-space, we use the two coordinate systems shown in Figure 1. The origin of the $y_1$ system is at the center of the slip zone a distance $h$ below the free surface. The $y_1$ and $y_2$ axes lie in the plane of the slip zone, and the $y_3$ axis is perpendicular to the slip surface. The $y_1$ axis is horizontal and points along one axis of the ellipse in the direction of the slip zone strike. The $y_2$ axis points along the other axis of the ellipse in the direction of slip zone dip and is inclined at an angle $\alpha$ from the vertical. Thus the slip zone dips at an angle $\pi/2 - \alpha$. The $x_i$ system has its origin at the surface directly above the center of the slip zone. The $x_1$ axis is horizontal, parallel to the $y_1$ axis, and in the direction of slip zone strike. The $x_2$ axis is vertical and points down into the half-space. The $x_3$ axis is horizontal and in the same vertical plane as the $x_2$ axis.

The kernel (8) can be calculated from *Mindlin*'s [1936] solution for a point force in an elastic half-space (also see *Mindlin* [1955] and *Mindlin and Cheng* [1950]) or, alternatively, by specializing the results of *Lee and Keer* [1986] and of *Lee et al.* [1987] for a bimaterial interface. The appendix records expressions for these kernels in components relative to the slip zone coordinate system $y_i$. The kernels of the integral (4) are also listed there in components relative to the half-space coordinate system $x_i$.

The numerical solution of the integral equation (7) follows the method developed by *Lee and Keer* [1986] for a tensile crack near a bimaterial interface. A feature of the method is that the variation of the relative displacements near the edge of the slipping zone is constrained to have the form appropriate for a crack in an isotropic linear elastic body. More specifically, the relative displacements near the crack edge have the following asymptotic form [e.g., *Rice*, 1968]:

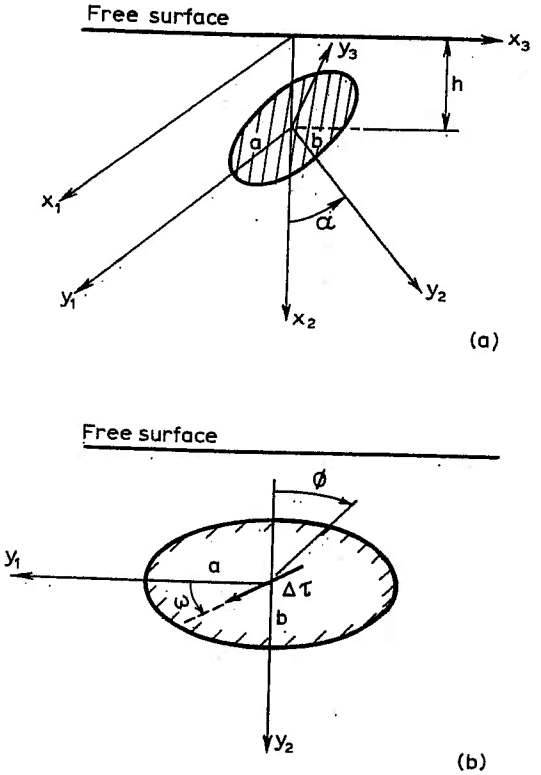


Fig. 1. (*a*) Geometry and coordinate systems for an inclined elliptical slip zone in the Earth's crust: The origin of the $y_i$ system is at the center of the slip zone a distance $h$ below the free surface. The $y_1$ and $y_2$ axes lie in the plane of the slip zone, and $y_3$ is perpendicular to the slip surface. The origin of the $x_i$ system is on the half-space surface directly above the slip zone center. The $x_1$ axis is parallel to $y_1$ and in the direction of slip zone strike, and the $x_2$ axis is perpendicular to the half-space surface. The angle between the vertical ($x_2$ axis) and the $y_2$ axis is $\alpha$. (*b*) View perpendicular to the plane of the slip zone ($y_1y_2$ plane). Polar angle $\phi$ is measured from the negative $y_2$ direction in the crack plane ($y_1y_2$). The orientation of the stress drop $\Delta\tau$ is defined by the angle $\omega$ measured from the $y_1$ (striking) direction.

$$(B_{\mathrm{I}}, B_{\mathrm{II}}, B_{\mathrm{III}}) = \frac{4(1-\nu)}{\mu}\left[\frac{\rho}{2\pi}\right]^{1/2}[K_{\mathrm{I}}, K_{\mathrm{II}}, K_{\mathrm{III}}/(1-\nu)] \tag{9}$$

as $\rho \to 0$, where $\rho$ is distance from the crack edge, $B_{\mathrm{I}}$ is the relative opening (mode I), and $B_{\mathrm{II}}$ and $B_{\mathrm{III}}$ are relative displacements for shearing perpendicular to (mode II) and parallel to (mode III) the crack edge. The constants $K_{\mathrm{I}}$, $K_{\mathrm{II}}$, and $K_{\mathrm{III}}$ are the corresponding stress intensity factors. Because the relative displacements near the edge of any crack in a linear elastic isotropic body have this form (9), any differences in geometry or applied loading are reflected entirely in different values of the stress intensity factors. The result (9) is embedded in the numerical solution by choosing the $B_i(\xi)$ to have the following form:

$$B_i(\xi) = [2a\varepsilon - \varepsilon^2]^{1/2} f_i(\xi) \tag{10}$$

where $\varepsilon$ is the shortest distance of the integration point $\xi$ to the crack front, and $a$ is the larger semiaxis of the elliptical slip zone [*Murakami and Nemat-Nasser*, 1983]. Hence resolving the $B_i$ near the crack edge into components perpendicular and parallel to the edge and comparing with (9) yields results for the stress intensity factors. Once the stress intensity factors have been determined, the energy release rate, that is, the energy released per unit area of advance of the slip zone, is expressed in terms of these factors as follows:

$$\mathbf{G} = \frac{(1-\nu)}{2\mu}[K_{\mathrm{I}}^2 + K_{\mathrm{II}}^2 + K_{\mathrm{III}}^2/(1-\nu)] \tag{11}$$

The numerical solution of (7) proceeds by dividing the slip surface into triangular domains in which $f_i(\xi)$ are assumed to be constant over each triangle. Imposition of the stress drop values at the centers of the triangular elements reduces (7) to a set of algebraic equations. For all cases to be considered here, the loading and geometry are symmetric with respect to the $y_2y_3$ plane; hence only half of the crack surface is used in solving (7). More specifically, for the results to be presented, the half-crack is divided into 80 triangular elements. The regular portions of the integrals over the triangles are evaluated numerically, but a combination of exact and numerical integration is used to treat the singular part [*Lee and Keer*, 1986]. *Lee and Keer* [1986] have shown that for a circular crack subjected to uniform pressure in an infinite body the mode I stress intensity factor calculated by this method has 0.85% error in comparison with the exact solution.

## EFFECT OF THE FREE SURFACE

Although the solution for an elliptical shear crack in an infinite space can be obtained by specializing results of *Eshelby* [1957] and has been studied in detail by *Kostrov and Das* [1984], there exist no analytical results for shear cracks in an elastic half-space. In this section we present results for the energy release rate, stress intensity factors, and moment for slip zones in an elastic half-space. For simplicity, we consider only elliptical cracks and constant stress drops, but the solution method, as described in the previous section, can treat arbitrary planar configurations and distributed stress drops. In order to examine the effects of the free surface, we compare the results with those for a crack of the same geometry and stress drop in an infinite space.

As shown in Figure 1, the model contains six parameters: the depth of the slip center $h$; the lengths of the principal semiaxes ($a$ and $b$); the inclination of the fault plane, defined by the angle $\alpha$ from the normal to half-space surface; the stress drop level $\Delta\tau$, and the stress drop direction, defined by the angle $\omega$ from the $y_1$ (striking) direction. The change in normal stress on the slip surface is specified to be zero. Two types of shear loading conditions are considered: the stress drop direction is parallel to the Earth's surface ($\omega = 0$), corresponding to strike-slip faulting; and the stress drop direction is along the dip direction of the fault ($\omega = +\pi/2$), corresponding to dip-slip (normal) faulting. For brevity, results for the stress intensity factors are presented only for an inclined ($\alpha = \pi/4$) circular slip zone with normal dip-slip loading ($\omega = \pi/2$). However, for the moment and energy release rates we consider both a circular crack and an elliptical crack with aspect ratio $a/b = 2$. For each crack shape we consider the following five possibilities: a deep vertical ($d/b = 3$; $\alpha = 0$), two moderately deep vertical ($d/b = 2$; $\alpha = 0$ and $d/b = 1$; $\alpha = 0$), a shallow vertical ($d/b = 0.1$; $\alpha = 0$), and a shallow inclined crack ($d/b = 0.1$; $\alpha = \pi/4$), where $d$ is the depth of the crack top (See inset of

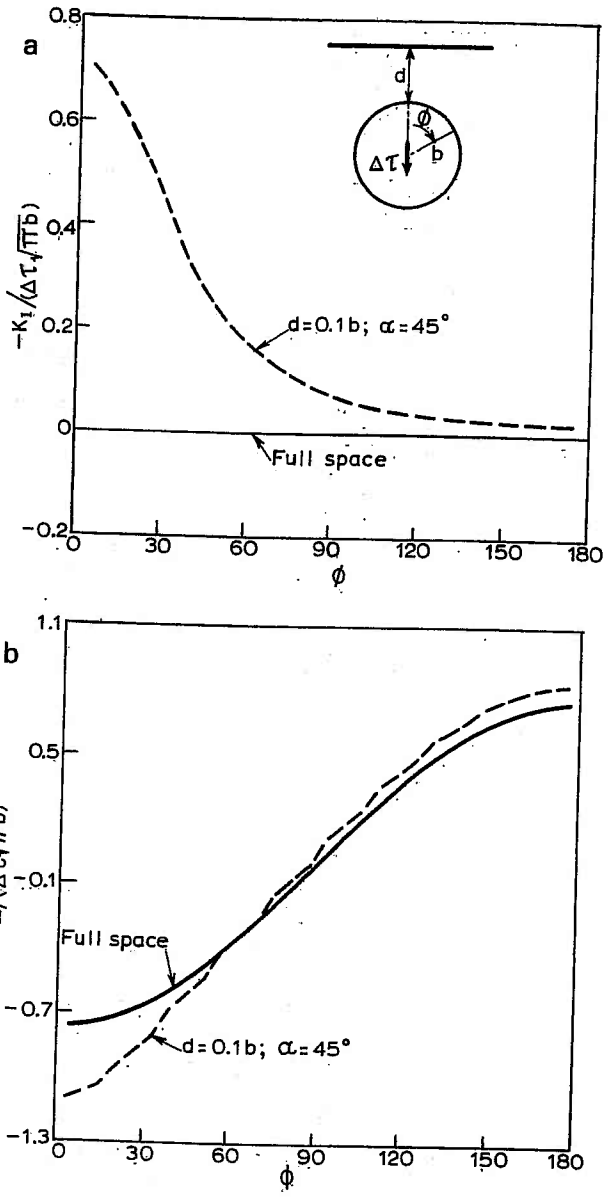


Fig. 2. Stress intensity factors (*a*) $K_I$, (*b*) $K_{II}$, and (*c*) $K_{III}$, divided by $\Delta\tau(\pi b)^{1/2}$, for a shallow inclined circular crack ($d = 0.1b$, $\alpha = 45°$; see inset in Figure 2*a*) against the polar angle $\phi$. The solid line shows the result for a crack of the same geometry in a full space. (Because $K_I < 0$, the negative of the stress intensity factor is plotted in Figure 2*a*.)

Figure 2*a*). In the calculations of the next two subsections, Poisson's ratio is taken to be 1/3, but $\nu = 1/4$ in the subsection on the moment.

### *Stress Intensity Factors*

As an example of the effect of the free surface on the stress intensity factors $K_I$, $K_{II}$, and $K_{III}$, we examine the solution for an inclined circular crack ($d/b = 0.1$; $\alpha = \pi/4$) subjected to normal dip-slip ($\omega = \pi/2$) loading. The stress intensity factors, divided by $\Delta\tau(\pi b)^{1/2}$, are plotted against the polar angle $\phi$ (defined in Figure 1) and compared with the corresponding full space results in Figures 2*a*, 2*b*, and 2*c*. For a crack in an infinite isotropic elastic body there is no coupling between slip and normal relative displacement. Consequently, the mode I (opening) stress intensity factor $K_I$ is identically zero, as shown in Figure 2*a*. However, the presence of the free surface causes a coupling between shear slip and normal relative displacement (in this case, interpenetration) and, as a result, $K_I$ is nonzero. The corresponding effect in two-dimensional problems was noted by *Dmowska and Kostrov* [1973] and has been discussed by *Dmowska and Rice* [1986].

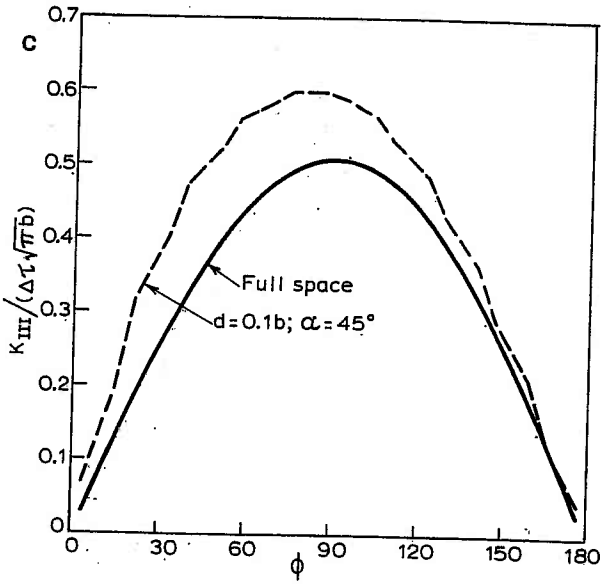


Fig. 2. (continued)

The magnitude of the effect diminishes with distance from the free surface and with the angle $\alpha$. For vertical slip zones, symmetry rules out the possibility of relative normal displacement. However, for inclined slip zones near the free surface the effect can be substantial. For results shown in Figure 2 the magnitude of $K_I$ at the shallowest point of the slip zone ($\phi = 0°$) is nearly 2/3 the maximum value of $K_{II}$, which also occurs at $\phi = 0°$.

In reality, interpenetration of the fault surfaces cannot occur and, except for slip zones very near the free surface, the ambient normal stress will presumably suppress any tendency for the slip to be accompanied by opening. The magnitude of normal stress changes can be estimated by solving (7) subject to the condition that $B_3 = 0$ (where $B_3$ is the relative displacement normal to the slip surface). Two of the equations (7) can then be solved for the slip components. Substituting these into the third yields the normal traction required to suppress any opening or interpenetration. In particular, for the crack shown in Figure 2 we found that the maximum compressive traction required to prevent interpenetration of the crack surfaces is about 87% of the applied shear stress drop. For this case, $K_{II}$ and $K_{III}$ differ from those shown in Figures 2*b* and 2*c* by less than 10% ($K_I$ is zero).

As discussed by *Dmowska and Rice* [1986], the coupling of normal relative displacement and slip near the free surface means that the shear stress drop alone cannot be specified a priori; if slip is assumed to be governed by Coulomb friction, then only a linear combination of the changes in normal stress and the shear stress can be specified. Although, as noted above, this effect can be significant near the free surface, for simplicity, we do not consider it further here.

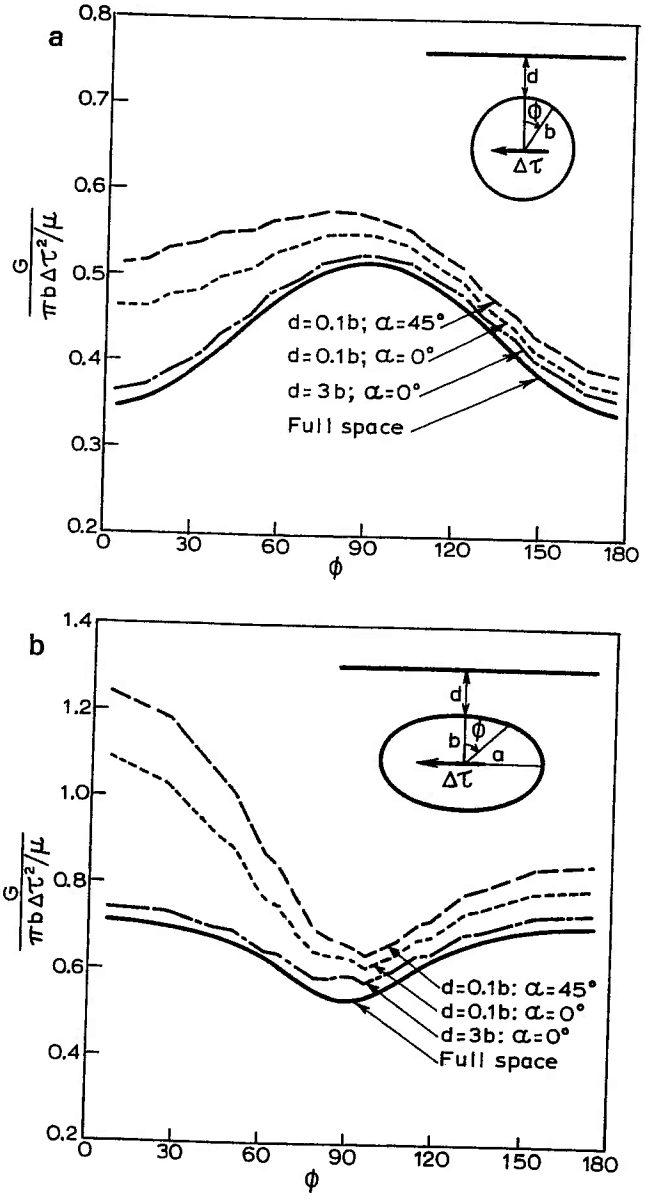


Fig. 3. Energy release rate G (11), divided by $\pi b\Delta\tau^2/\mu$, against $\phi$ for (*a*) circular and (*b*) elliptical (aspect ratio $a/b = 2$) slip zones subjected to strike-slip loading.

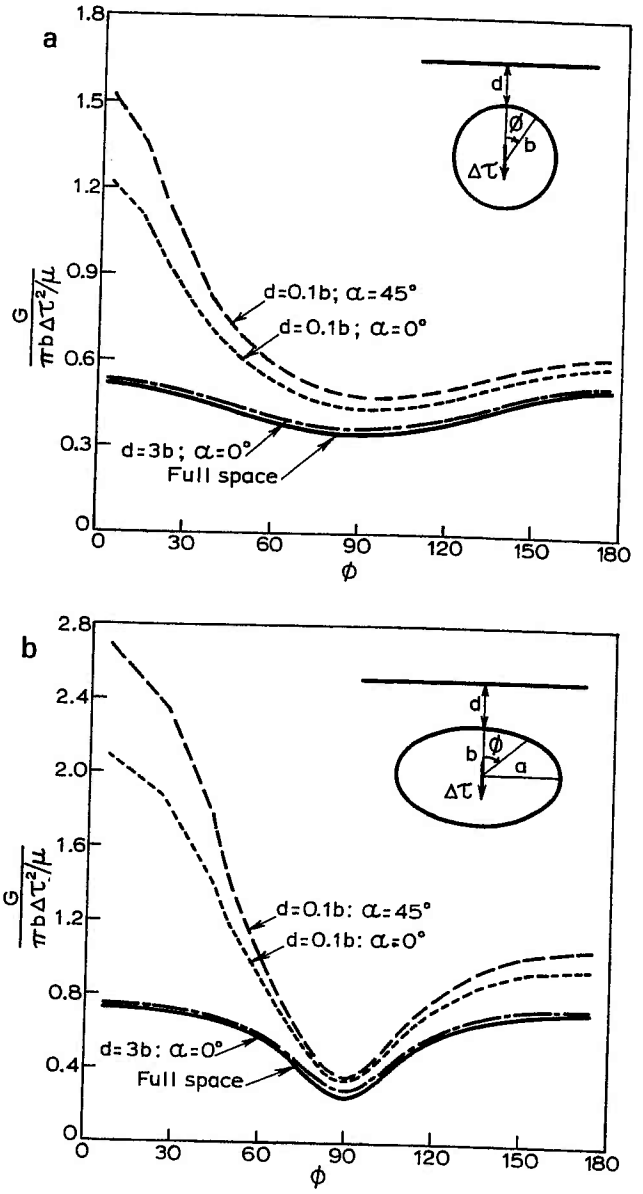


Fig. 4. Energy release rate G (11), divided by $\pi b\Delta\tau^2/\mu$, against $\phi$ for (*a*) circular and (*b*) elliptical (aspect ratio $a/b = 2$) slip zones subjected to dip-slip loading.

### *Energy Release Rate*

Although it is instructive to consider the stress intensity factors individually, only the combination defined by (11) enters the expression for the energy release rate. Figures 3 and 4 plot the variation of the energy release rate G, divided by $\pi b\Delta\tau^2/\mu$, against the polar angle $\phi$ for different crack configurations for the cases of strike-slip and normal dip-slip motion. As indicated in these figures, the distributions of the normalized energy release rate for the deep slip zones ($d/b = 3$) are about the same as for the corresponding full-space sources, as expected. Only when the ratio $d/b = 1.0$ do the results differ by as much as 10% from those for the full space solutions. The energy release rates for the shallow slip zones, however, can differ significantly from the full space results, depending on the configuration and loading condition. Overall, the free-surface effect is greater for dip slip than for strike slip, given the same crack geometry.

For both the circular (Figure 3*a*) and the elliptical slip (Figure 3*b*) zones with strike-slip loading, the variation of the energy release rate with $\phi$ is similar to that for the same slip zone in an infinite body. For the circular zone the energy release rate is largest at the side ($\phi = 90°$) and decreases toward the top ($\phi = 0°$) and bottom ($\phi = 180°$). For the elliptical crack with aspect ratio $a/b = 2$, the energy release rate is greatest at the edge nearest the free surface and least at the side of the slip zone ($\phi = 90°$). The presence of the free surface causes G to increase for both the circular and elliptical zone with the greatest increase occurring nearest to the free surface. More specifically, for shallow dipping zones the energy release rate induced by the shallow vertical crack ($d/b = 0.1$; $\alpha = 0$) is greater than that for the full space source by about 33% near the top of the crack ($\phi \simeq 0$) and by less than 7% along the portion of the crack front away from the free surface of the Earth ($\phi > 90°$). When this shallow

source dips at 45° ($d/b = 0.1$; $\alpha = 45°$), the difference is increased about 15%. For the elliptical geometry (strike slip; $a/b = 2$), even larger differences (50% and 70%) occur for the shallow vertical ($d/b = 0.1$; $\alpha = 0$) and shallow inclined crack ($d/b = 0.1$; $\alpha = 45°$) (Figure 3*b*).

The difference in the variation of the energy release rates with $\phi$ for the circular and elliptic slip zones can be understood in terms of the behavior of the stress intensity factors for the full space solution [*Kostrov and Das*, 1984]. At $\phi = 0°$ (and 180°) the solution is pure mode III ($K_{II} = 0$), and at $\phi = 90°$ the solution is pure mode II ($K_{III} = 0$). As discussed in detail by *Kostrov and Das* [1984], the ratio of the mode II stress intensity factor at $\phi = 90°$ to the mode III stress intensity factor at $\phi = 0°$ (and 180°) is $(b/a)^{1/2}/(1 - \nu)$. Hence the corresponding ratio of the energy release rate at $\phi = 90°$ to that at $\phi = 0°$ is $(b/a)/(1 - \nu)$. Thus, for the circular slip zone, G at $\phi = 90°$ is 1.5 times that at $\phi = 0°$ (for $\nu = 1/3$). For the elliptical slip zone with aspect ratio $a/b = 2$, G at $\phi = 90°$ is 0.75 times that at $\phi = 0°$.

If the slip zone is assumed to spread in the direction of the greatest energy release rate, then the results of Figure 3*a* suggest that an initially circular zone propagates horizontally rather than toward the free surface. However, Figure 3*b* shows that an increase in the aspect ratio $b/a$ increases the energy release rate both at the top and bottom of slip zone ($\phi = 0°$, 180°), but the increase is greater at the top near the free surface. Thus, for an initially circular slip zone, horizontal propagation would be followed by propagation toward the free surface before the aspect ratio reached $b/a = 2$. For an initially elliptical slip zone (with $b/a \geq 2$), propagation would occur first toward the free surface.

Figures 4*a* and 4*b* show the variation of the energy release rate with $\phi$ for dip-slip loading of circular (Figure 4*a*) and elliptical slip zones. As for the strike-slip loading, the variation is similar to that for the full space solutions. For both the circular and elliptical zones, G is least at $\phi = 90°$ and increases toward the top and bottom of the slip zone. For shallow zones the dip-slip loading causes a particularly large increase of G toward the free surface. Specifically, for a shallow ($d = 0.1b$) vertical ($\alpha = 0$), circular slip zone, the values exceed those for the full space solution by about 150% near the free surface and by 20% away from the free surface. For the inclined shallow circular crack ($d/b = 0.1$; $\alpha = 45°$) the difference is about 18% larger. Figure 4*b* shows that the energy release rates for the vertical ($\alpha = 0°$) elliptical crack at a depth of $d = 0.1$b exceed those for the full space by even larger amounts: 200% near the top of the crack and 38% near the bottom. For the inclined shallow elliptical crack ($d/b = 0.1$; $\alpha = 45°$) the difference can be as large as 250%. Because the maximum energy release rates all occur at the top of the slip zone for these two geometries, dip-slip rupture would tend to break to the surface rather than grow along strike.

### *Moment*

The stress intensity factors and energy release rates arise naturally in considering crack models of slip zones. But a parameter more commonly used in interpreting observations is the seismic moment. Because the stress drop is specified in the approach used here, the slip distribution and hence the moment are calculated as part of the solution.

In this subsection we examine the effect of the free surface on the relation between the moment and the stress drop. In particular, consider the single component of the moment tensor given by

$$M = \mu \int_S B_\tau(\xi)\, d\xi \tag{12}$$

where $B_\tau$ is the relative slip in the direction of the applied stress drop (Figure 1). Hence $M$ is the component $M_{31}$ or $M_{32}$ in the crack coordinate system ($y_i$), depending on whether the loading is strike slip or dip slip, respectively; similarly, $B_\tau$ is $B_1$ or $B_2$ depending on the loading. In general, the slip will also have a component orthogonal to the applied stress drop. For example, *Kostrov and Das* [1984] have shown that for an elliptical shear crack in an infinite body the slip is parallel to the applied shear stress only if the latter is applied in the direction of one of the principal axes of the ellipse. In the half-space problems considered here the slip will be in the direction of the applied shear stress only when the problem is symmetric with respect to the loading direction. The magnitude of the slip orthogonal to the applied stress is, however, much smaller than that in the direction of the shear stress. In addition, as noted previously, when the change in normal traction on the slip surface is taken as zero, there is a normal relative displacement, and hence $M_{33}$ is nonzero. However, unless the slip surface is very near the free surface, this component is also small and, for simplicity, we ignore it.

For constant stress drop slip zones the moment $M$ (equation (12)) is proportional to the stress drop $\Delta\tau$ and can be expressed as follows:

$$M = C\, \Delta\tau\, A^{3/2} \tag{13}$$

where $A$ is the area of the slip surface and $C$ is a nondimensional quantity that depends on Poisson's ratio and the geometry. For example, for a circular slip zone in an infinite space, $C$ is

$$C = \frac{16(1 - \nu)}{3\pi^{3/2}(2 - \nu)} \tag{14}$$

For an elliptical slip zone in an infinite body with principal semiaxes $a$ and $b < a$, $C$ is given by

$$C = \frac{4}{3\pi^{1/2}}\, k_1^{1/2} k^2 [(k^2 - \nu)E(k) + \nu k_1^2 K(k)]^{-1} \tag{15}$$

if $\Delta\tau$ is applied parallel to the larger semiaxis, and by

$$C = \frac{4}{3\pi^{1/2}}\, k_1^{1/2} k^2 [(k^2 + \nu k_1^2)E(k) - \nu k_1^2 K(k)]^{-1} \tag{16}$$

if $\Delta\tau$ is applied parallel to the smaller semiaxis [*Dmowska and Rice*, 1986]. In (15) and (16), $k_1 = b/a$, $k = 1 - k_1^2$, and $E(k)$ and $K(k)$ are complete elliptic integrals of the first and second kinds, respectively.

The expression (13), with $C$ given by (14), is often used to estimate the stress drop when the moment is determined by kinematic models. As noted earlier, for kinematic models using constant relative displacement elements, the actual average stress drop is unbounded. Furthermore, the value of $C$ given by (14) is for an infinite space. Consequently, it is of interest to determine the effect of the free surface on the

TABLE 1. Values of $C = M/(\Delta\tau A^{3/2})$

| | Strike Slip ($\omega = 0°$) | | Dip Slip ($\omega = 90°$) | |
|---|---|---|---|---|
| | $a/b = 1$ | $a/b = 2$ | $a/b = 1$ | $a/b = 2$ |
| Full space | 0.4105 | 0.4042 | 0.4105 | 0.3523 |
| $d/b = 3$; $\alpha = 0°$ | 0.4169 | 0.4180 | 0.4177 | 0.3630 |
| $d/b = 0.1$; $\alpha = 0°$ | 0.4327 | 0.4473 | 0.4823 | 0.4488 |
| $d/b = 0.1$; $\alpha = 45°$ | 0.4481 | 0.4707 | 0.5117 | 0.4810 |

value of $C$ and hence the effect on inference of the stress drop from the moment by (14).

Table 1 lists the values of $C$ for the slip zones considered in Figures 3 and 4 and the corresponding values for a slip zone of the same geometry and loading in an infinite space. Poisson's ratio of $\nu = 0.25$ is used for these calculations. Values of $C$, using (12) and (13), for the deep cracks ($d/b = 3$) differ by less than 3% from those, using (14)–(16), for the full space cracks of the same geometries and stress drops. For the vertical shallow cracks, the half-space moments differ from the corresponding full space results by 6% for the circular and 11% for the elliptical crack for the case of strike slip and by 18% for the circular and 27% for the elliptical crack for the case of dip slip, respectively. For the inclined shallow cracks, additional differences up to 10% are observed. Because of the coupling between the shear slip and the normal relative displacement, the moment component $M_{33}$ (along the normal direction of the crack surface) can be as large as about two thirds of the larger shear component.

## INTERPRETATION OF COSEISMIC SURFACE DEFORMATIONS

As examples of the application of this method, we use it to reexamine the coseismic surface deformations of three earthquakes: 1987 Whittier Narrows, 1983 Borah Peak, and 1966 Parkfield. The coseismic deformations for these earthquakes have been studied previously using kinematic models. The present approach differs from those previous because the geometry and the stress drop, rather than the slip distribution, are inferred from the observations. The slip distribution is then calculated for the inferred stress drop and geometry.

For each earthquake a set of forward searches is performed to find the model parameters that give a best fit to the coseismic slip data subject to the constraint that the model geometry agrees roughly with the aftershock distribution. Then, by using the stress drop and crack geometry determined from a best model, the corresponding slip moment and energy release rate are calculated and compared, together with the model parameters, with those inferred from previous studies. The results are summarized in Table 2. For the calculations in this section, a Poisson's ratio $\nu = 0.25$ and a shear modulus $\mu = 3 \times 10^4$ MPa, an average value for the Earth's crust, are assumed.

### *1987 Whittier Narrows*

The 1987 Whittier Narrows earthquake occurred within the Los Angeles basin in southern California. The geologic and tectonic setting have been described by *Davis et al.* [1989]. The coseismic surface elevation changes were detected by geodetic surveys [*Lin and Stein*, 1989]. A crosslike geodetic network, centered coincidentally on the epicenter, was surveyed 20 months before the earthquake and resurveyed immediately after. The surveys reveal that the ground surface was uplifted by 50 mm, but no surface rupture was observed. *Lin and Stein* [1989] used a model of an inclined rectangular dislocation of uniform dip slip in an elastic half-space [*Mansinha and Smylie*, 1971] to interpret the observed deformation as due to reverse dip slip of a deep thrust fault beneath the center of the network. Because the geodetic data alone cannot constrain the fault geometry and slip magnitude uniquely, *Lin and Stein* [1989] also considered the aftershocks which occupied a region extending from the depth of 12 km to 16 km. For their best model, the fault length along strike is 4.5 km, the downdip width is 6 km, the depth of the upper end of the fault plane is 12 km, the dip angle is 30°, and the coseismic slip is 1.1 m.

Here we employ an alternative approach to interpret coseismic deformation reported by *Lin and Stein* [1989]. Specifically, we model the event as reverse dip slip of an inclined elliptical slip zone in an elastic half-space and assume a stress drop along the negative dip direction (Figure 1: $\omega = -90°$). For the best model, which matches the deformation data well and is consistent with the aftershock locations, the slip zone is circular with a radius of 3.0 km, the depth of the fault center is 14.2 km, and the dip angle is 40°. The total rms misfit is 5.8 mm, slightly larger than the rms pure error, which is 4.9 mm. The surface projection of the fault plane of our preferred model is shown in Figure 5*a*; the

TABLE 2. Comparison Between Modeling Results

| | Whittier Narrows ($M = 6.0$) | | Parkfield ($M = 5.6$) | | Borah Peak ($M = 6.9$) | |
|---|---|---|---|---|---|---|
| | *Lin and Stein* [1989] | This Study | *King et al.* [1987] | This Study | *Barrientos et al.* [1987] | This Study |
| Length (along strike), km | 4.5 | 6.0 | 30 | 50 | 18 and 8 | 36 |
| Width (downdip), km | 6.0 | 6.0 | 5 | 14 | 18 and 8 | 18.5 |
| Depth (to rupture top), km | 12 | 12.3 | 3 | 1.75 | 0 | 0 |
| Dip | 30°N | 40°N | 90° | 90° | 49°SW | 50°SW |
| Strike | N90°E | N90°E | ... | N142°E | N152°E | N152°E |
| Slip, m | 1.09 | 1.0/1.5 (ave/max) | 0.91 | 0.5/0.76 (ave/max) | 2.1 and 1.4 | 1.4/2.2 (ave/max) |
| Stress drop, MPa | 17.5 | 16 | ... | 1.43 | 3.0 | 1.8 |
| Moment, dyn cm | $1.0 \times 10^{25}$ | $0.96 \times 10^{25}$ | $4.5 \times 10^{25}$ | $7.2 \times 10^{25}$ | $2.9 \times 10^{26}$ | $2.4 \times 10^{26}$ |
| G, J/m$^2$ | ... | $2 \times 10^8$ | ... | $1.5 \times 10^6$ | ... | $1.2 \times 10^6$ |
| rms/pure error | 0.93 | 1.18 | ... | 0.97 | 2.5 | 6 |

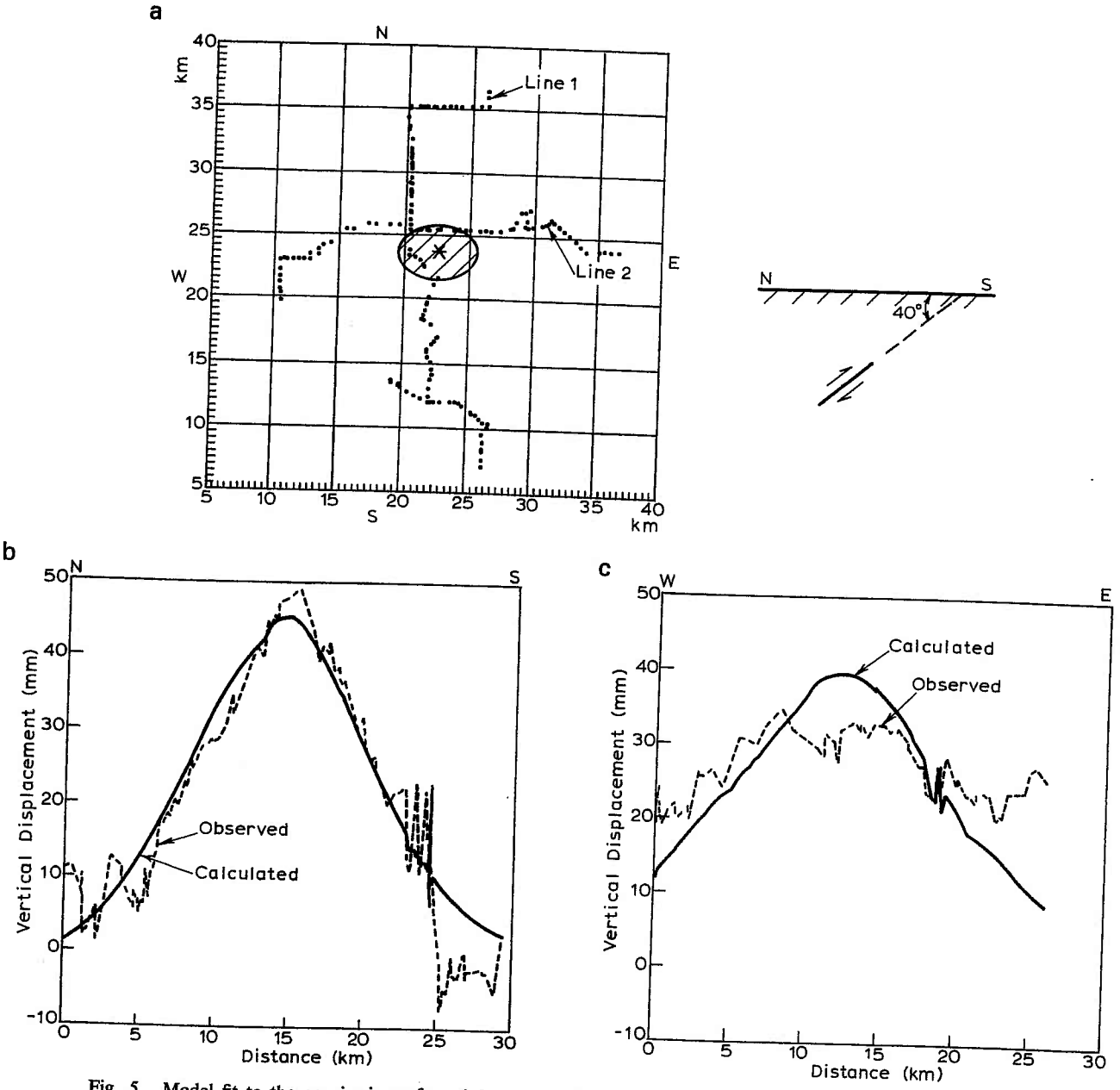


Fig. 5. Model fit to the coseismic surface deformation of the 1987 Whittier Narrows earthquake. (*a*) Leveling monuments and the surface projection of the model fault. Asterisk represents the epicenter of the earthquake. (*b*) Fit to data along leveling line 1. (*c*) Fit to data along leveling line 2.

model fits to data along two leveling routes, line 1 (N-S) and line 2 (E-W), are shown in Figures 5*b* and 5*c*, respectively.

As shown in Figure 5*b*, the predicted surface displacement agrees well with the observed data along line 1 except at the southern end. The fit to data is not as good along line 2 but is still satisfactory (Figure 5*c*). These results are similar to those of *Lin and Stein* [1989]. The stress drop and moment determined for the preferred model are 16 MPa and $0.96 \times 10^{25}$ dyn cm, respectively, compared with the 17.5 MPa and the $1.0 \times 10^{25}$ dyn cm determined by Lin and Stein. Because the ratio of the depth to slip zone radius is relatively large ($\simeq$4), the energy release rate for this model is approximately constant along the fault front and is essentially identical to that for a slip zone of the same geometry and stress drop in an infinite body. The value is estimated to be about $2.0 \times 10^8$ J/m$^2$.

The dipping angle (40°) of our best model is about 10° larger than inferred by Lin and Stein using their dislocation method. If we use the same dip (30°) as theirs, the rms error is increased to 6.3 mm. The coseismic slip data are not critically sensitive to the radius of the slip region. More specifically, the area can be varied from moderately larger (radius 5 km) to much smaller (radius 1 km) than that defined by the aftershock distribution without affecting the rms error significantly. In addition, while keeping the width (along dip) of the fault to be 5 km, horizontal length of slip up to 16 km is permitted by the deformation data. Because the ratio of depth to slip region radius is large, the uplift data can be fit reasonably well by a point source. For the point dip-slip source having the same inclination, depth, and moment as the best crack model, the uplift data can be fitted with the

TABLE 3. Observed and Calculated Line Length Changes

| Station-Station | Observed, mm | Calculated, mm | Residual, mm |
|---|---|---|---|
| Bench-Bonnie | −69 ± 24 | −78.3 | 9.3 |
| Bench-Cotton | 42 ± 19 | 51.2 | −9.2 |
| Bench-Kenser | −137 ± 24 | −163.4 | 26.4 |
| Bench-Mason | 30 ± 18 | 13.6 | 16.4 |
| Bonnie-Cotton | 27 ± 18 | −16.3 | 43.3 |
| Bonnie-Kenser | 5 ± 16 | −4.2 | 9.2 |
| Bonnie-Mason | 81 ± 24 | 85.5 | −4.5 |
| Castle-Shade | 115 ± 38 | 88.8 | 26.2 |
| Cotton-Kenser | −5 ± 24 | −24.9 | 19.9 |
| Cotton-Mason | 167 ± 26 | 159.6 | 7.4 |
| Kenser-Mason | −7 ± 20 | −27.1 | 20.1 |
| Mine Mountain-Shade | 58 ± 18 | 65.4 | −7.4 |
| Park-Red Hill | −160 ± 24 | −124.4 | −35.6 |

Mean misfit (rms) = 21.4 mm.

rms error of 6.4 mm, only 10% larger than the crack model's misfit.

### *1966 Parkfield*

Trilateration measurements made by several agencies since 1959 near Parkfield provide geodetic data that place constraints on the motion across the San Andreas fault [*King et al.*, 1987]. Line length changes observed shortly after the 1966 Parkfield earthquake in that area have been the focus of much effort. Several investigators modeled the 1966 shock as a vertical rectangular dislocation of uniform strike slip in an elastic half-space [e.g., *Chinnery*, 1961]. Distributed dislocation models were also considered by approximating the slip as uniform in small rectangular cells [*Stuart et al.*, 1985; *Segall and Harris*, 1987]. However, because there were only 13 lines near the 1966 rupture zone, the length, depth, and width of the slip region cannot be constrained strongly by the geodetic observations alone [*King et al.*, 1987; *Segall and Harris*, 1987].

Additional constraints come from the distribution of aftershocks, which were concentrated at depths of 2–4 and 8–10 km on a nearly vertical plane extending 30 km SE of the main shock epicenter [*Eaton et al.*, 1970]. The absence of surface offset immediately following the main shock [*Smith and Wyss*, 1968] indicates that the 1966 coseismic slip probably did not reach the Earth's surface. Therefore most coseismic slip models have used a rupture geometry that extends from a depth of 2–4 km to a depth of 8–10 km with the length ranging from 20 to 40 km [*Archuleta and Day*, 1980; *King et al.*, 1987; *Segall and Harris*, 1987].

We propose a model of a vertical elliptical crack embedded in an elastic half-space. The surface of the crack is subjected to a uniform shear stress drop along the strike direction (Figure 1; $\alpha = 0$ and $\omega = 0$). The fit of the preferred model to the line length changes [*King et al.*, 1987] is provided in Table 3. The trilateration net and the surface trace of the model slip zone are shown in Figure 6. The surface center of the model fault is located near the middle point of the line connecting Mason and Kenger stations, the strike direction is nearly parallel to that of the line of Mason and Bench stations, and the top, the bottom, and the horizontal length of the fault are 1.75, 15.75, and 50 km, respectively (Table 2 and Figure 6). Although the area of the model rupture plane is moderately larger than the region

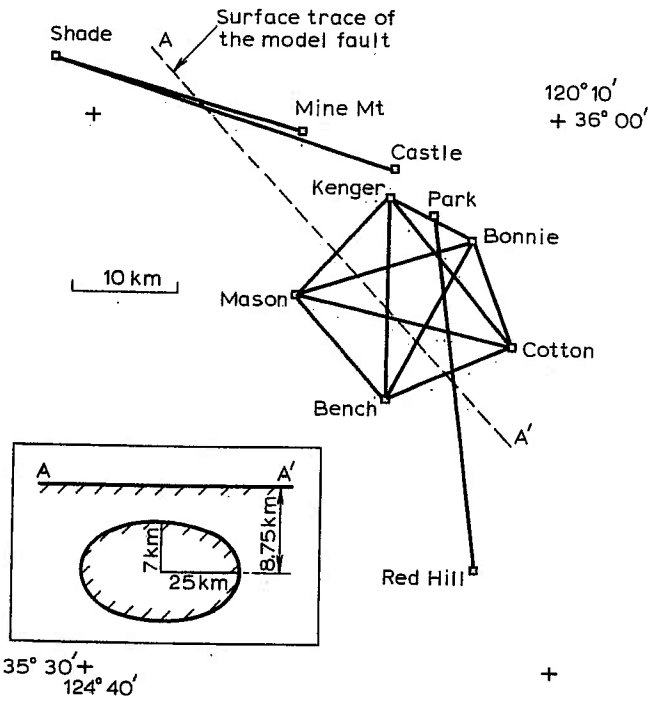


Fig. 6. Trilateration net and surface trace of the model slip zone inferred for the 1966 Parkfield earthquake.

defined by the aftershocks, the mean misfit to the data is significantly smaller (20% less) than models having slip areas much less than the aftershock region. The mean misfit of the preferred model to the data is 21.4 mm, lower that the average standard deviation of the data, which is 22.5 mm (Table 3). The only significant misfit occurs for the line connecting Bonnie and Cotton stations (Table 3). The observed line length change is 27 mm; the predicted value is −16 mm, close to the −10 mm predicted by *Segall and Harris* [1987] using a distributed dislocation model. The reason for this misfit is uncertain.

The stress drop and moment determined are about 1.43 MPa and $7.2 \times 10^{25}$ dyn cm, respectively. Our estimated moment is larger than the $4.5 \times 10^{25}$ dyn cm obtained by *King et al.* [1987] using the dislocation approach (Table 2) and the $(0.9–2.1) \times 10^{25}$ dyn cm inferred from surface waves by *Tsai and Aki* [1969] but falls within the range of $(3.7–8.1) \times 10^{25}$ dyn cm estimated by *Segall and Harris* [1987] using a distributed dislocation model. The maximum energy release rate occurs near the top of the slip zone and is estimated to be approximately $1.5 \times 10^6$ J/m$^2$. This value is consistent with the $0.8 \times 10^6$ J/m$^2$ estimated by *Aki* [1978] as corresponding to arrest of this earthquake but much greater than the estimate by *Husseini et al.* [1975] of $1.1 \times 10^2$ J/m$^2$.

If the area of the slip region is constrained so that its top, bottom, and horizontal length vary between 2–4, 8–10, and 20–40 km, where the aftershocks concentrated, then the model that fits the data best occupies the largest possible area. The mean misfit of this model to the data is 27 mm. Better fits are obtained when the rupture zone extends below the region of aftershocks to about 16 km depth. The coseismic line length changes permit slip extending even deeper than 16 km. The Park-Red Hill and Castle-Shade line length changes are much more sensitive to the horizontal length of

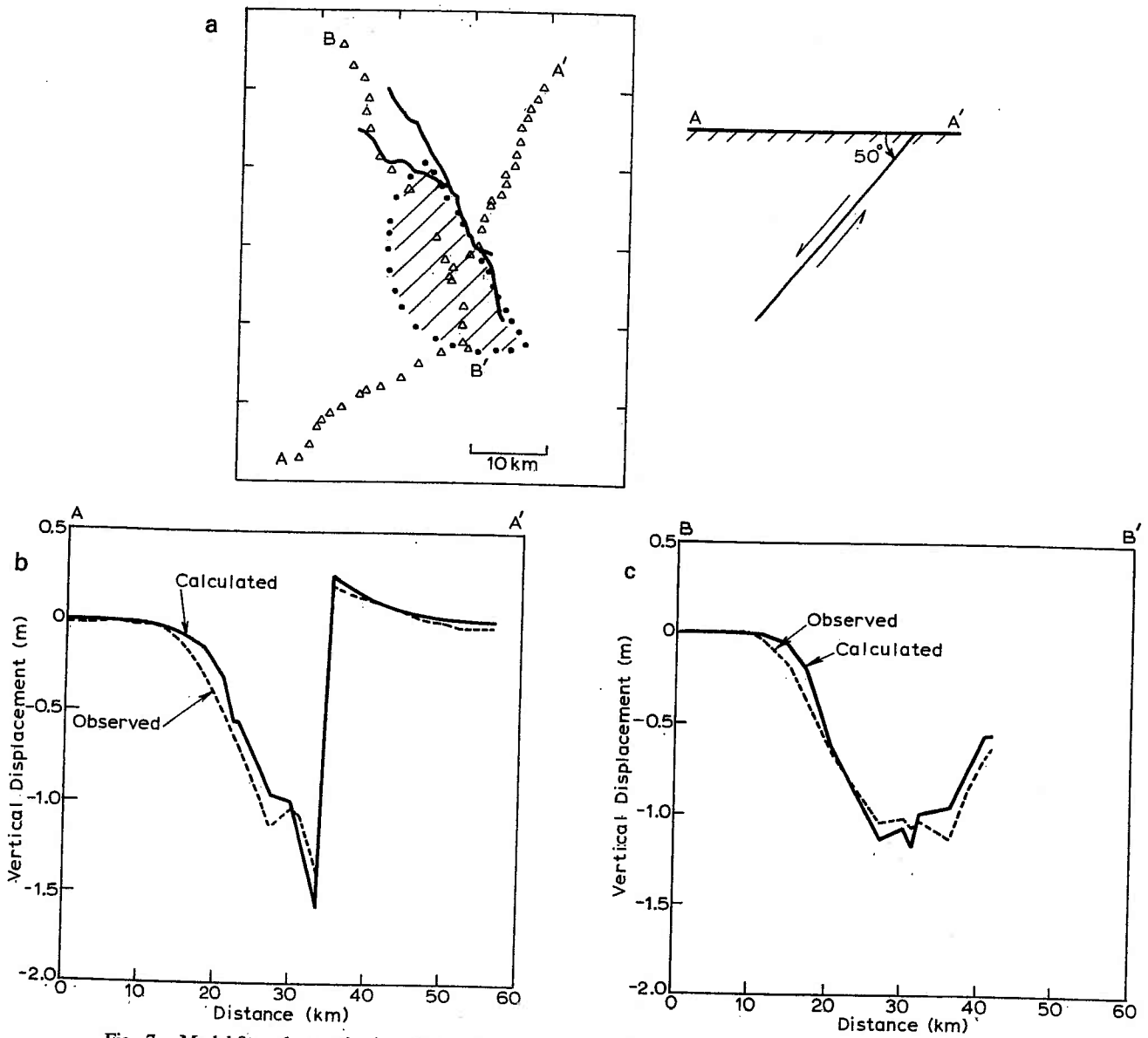


Fig. 7. Model fit to the coseismic surface deformation of the 1983 Borah Peak earthquake. (*a*) Leveling monuments and the surface projection of the model fault. (*b*) Fit to data along leveling line AA′ (pure error = 12 mm). (*c*) Fit to data along leveling line BB′ (pure error = 12 mm).

the slip region than other lines. Model fit can be degraded significantly for slip zones with horizontal lengths much shorter than 40 km, but longer length is permitted by the data. These results are in agreement with those of *King et al.* [1987].

### *1983 Borah Peak*

The Borah Peak segment of the Lost River fault lies in the northern Basin and Range Province. The 1983 Borah Peak earthquake, a large normal-faulting event, presumably resulted from regional extension of the Basin and Range. The earthquake ruptured the central 35-km segment, the length of the surface rupture trace, of the 100-km-long Lost River fault [*Barrientos et al.*, 1987].

The surface deformation associated with this event was reported by *Stein and Barrientos* [1985]. Two leveling lines, with line AA′ nearly normal to the fault and line BB′ about parallel to the main fault trace, were surveyed in 1933 (Figure 7*a*). Line AA′ was surveyed again in 1948. Both lines were resurveyed in 1985. Thus the survey includes 20 months of deformation following the earthquake. *Stein and Barrientos* [1985] have shown that the 1983–1984 postseismic slip is about 2% of the coseismic slip. By using dislocation models, *Barrientos et al.* [1987] studied the 1933–1948 preseismic deformation and the 1985 postseismic data to invert for the subsurface fault geometry and slip magnitude at Borah Peak. In their inversion procedure the strike of rupture planes was fixed to be consistent with the fault trace. Their best model consists of two planes of the same dip and strike: an 18 × 18 km main plane with 2.1 m slip and an 8 × 8 km second plane with 1.4 m slip located along strike northwest of the main plane. The dip angle of the planes is 49°. The rms misfit is 30 mm, 2.5 times the data noise level. This geometry agrees well with the focal mechanism of the

main shock [*Doser and Smith*, 1985] and the aftershock distribution [*Richins et al.*, 1985].

We use a dip-slip crack model to reexamine the surface deformation associated with this 1983 earthquake. Because the fault ruptured to the surface in the Borah Peak event, the dip-slip zone is approximated by a semielliptical geometry. For the parameters shown in Figure 1 we take $\omega = 90°$ and $h = 0$. As shown in Table 2, the strike (150°) and dip (50°) of our best model are similar to those of *Barrientos et al.* [1987], but the surface center of the slip zone is 3 km SE of theirs. The horizontal length of 36 km and width along dip of 18.5 km for our model are larger than but close to those (26 km and 18 km) for their best model. Normal dip slip is required over the surface of the fault. Figure 7*a* shows the surface projection of the model fault plane; Figures 7*b* and 7*c* indicate the model fit to data along line AA′ and line BB′, respectively.

Overall, the predicted values roughly match the observations. However, the predicted displacement significantly overshoots the maximum elevation change and moderately underestimates the other large elevation changes for line AA′. For line BB′ the predicted displacement moderately overestimates about half of the data and underestimates the other half data. The rms error of the fit to data is large, about 70 mm, 6 times the rms pure error. The better fit obtained by *Barrientos et al.* [1987] using the distributed slip model and the pattern of the discrepancy between the predictions here and observations on line AA′ suggest that the constant stress drop assumption needs to be relaxed in order to improve the fit to the data: uniform stress drop constrains the slip to be distributed roughly elliptically, and therefore the slip is largest at the center and tapers to zero at the edge. However, because the purpose here is to illustrate the approach and to provide estimates for the slip-induced energy release rate rather than fit the data precisely, we have not pursued nonuniform stress drop models.

The stress drop and moment determined by our best model are 1.8 MPa and $2.4 \times 10^{26}$ dyn cm, respectively, smaller than the 3.0 MPa and $2.9 \times 10^{26}$ dyn cm inferred by Barrientos et al. using a single-plane model which is 18 km in width and 23 km in length (No stress drop and moment values were reported for their two-plane model). The maximum (calculated) energy release rate occurs at the ends of the surface trace of the rupture and is estimated to be $1.2 \times 10^6$ J/m$^2$.

Because this event breaks the surface, there is a strong coupling between slip and normal relative displacement. Because we have specified zero normal stress change on the slip surface in (6), the fault surfaces are predicted to interpenetrate. For the best fitting model the predicted interpenetration is about 1.6 m at the surface, 73% of the maximum relative displacement along dip, and decreases to zero at the deepest portion of the fault. Of course, in actuality, the fault will not interpenetrate because the normal stress will increase in compression. To estimate the magnitude of the normal stress change, we repeated the calculation but required that the normal relative displacement be zero. (This change has negligible effect on the fit of the leveling data.) The resulting normal traction is compressive (tending to open the crack) over most of the fault surface with a maximum value of about 110% of the applied shear stress drop occurring at the surface. Surprisingly, a small tensile stress (about 7% of the applied shear) is required on the deepest portions of the fault. Apparently, this occurs because preventing interpenetration of the crack faces near the surface tends to cause the deeper portions to open. A more complicated analysis that includes the effect of the change in normal stress on the resistance to slip is needed to determine more accurately the magnitude of the normal stress changes. However, these limiting cases suggest that the effect can be significant.

## CONCLUDING DISCUSSION

In this paper we have described a numerical method for determining the displacements in an elastic half-space caused by slip on planar zones in response to a prescribed shear stress drop. Although, for simplicity, we have presented results only for uniform stress drops and elliptical slip zones, the method can be applied to arbitrarily shaped planar zones and distributed stress drops. By incorporating the appropriate asymptotic form of the displacement field near the edge of a crack in a linear elastic isotropic body, we are able to calculate accurately the stress intensity factors and hence the energy release rates. These quantities can be used in propagation criteria for determining the advance of the slip zone.

Because so few solutions exist for crack models of slip zones in a half-space, the magnitude and nature of the effect of the free surface have been uncertain. To examine this effect, we have presented results for the stress intensity factors and energy release rates for slip zones of various shapes, depths, and inclinations and compared them with solutions for slip zones of the same shape in an elastic full space. Although the details depend on the specific geometry, in general, when the distance of the slip zone center from the free surface ($h$) is greater than the downdip width of the slip zone ($2b$), the difference between the half-space and full space results is less than 10%. In addition, the influence of the free surface increases with decreasing dip angle.

We have also examined in detail the effect of the free surface on the relation between the seismic moment and the stress drop (see (13) and Table 1). The seismic moment is a relatively well-determined observational parameter, and the relation between the stress drop and the moment for a circular or elliptical crack in an infinite elastic body is often used to infer the stress drop. Again, the results indicate that the effect of the free surface is small (less than about 10%) unless the fault rupture is very near to the free surface ($h$ less than the downdip width $2b$). The effect can, however, be significant for dipping faults that rupture to (or nearly to) the free surface.

Another effect of the free surface revealed by the calculations here is the coupling of slip with normal relative displacement which has been noted previously in two-dimensional problems by *Dmowska and Kostrov* [1973]. Because of this coupling, the shear resistance, which is proportional to the normal stress for a simple Coulomb condition, is coupled to the slip. Consequently, as remarked by *Dmowska and Rice* [1986], it is not possible to specify the shear stress drop a priori, and iteration is necessary to obtain the solution for a given shear stress drop. Although we have not pursued a full analysis of this coupling, some insight can be gained from consideration of the limiting cases in which either the normal stress change on the fault or the normal relative displacement is specified as zero.

When the change in normal stress is specified to be zero (as has been the case here, except where noted), the calculations indicate that the surfaces of reverse dip-slip faults tend to open and those of normal dip-slip faults tend to interpenetrate. (Actual interpenetration is prevented by an increase in normal compressive stress, and opening is opposed by the ambient compressive stress). Conversely, if the relative normal displacement is required to be zero, slip induces changes in normal stress. For reverse slip the change in normal stress is tensile (tending to prevent opening) over most of the rupture. For normal dip-slip motion the normal stress changes are compressive over most of the slip surface.

As example applications of the solutions, we have used them to reexamine surface deformation data from the 1987 Whittier Narrows, 1973 Borah Peak, and 1966 Parkfield earthquakes. In all three cases the geometries, stress drops, and moments inferred are similar to those obtained previously by others using kinematic models. The agreement lends additional confidence in the previous results, and the slight differences give an indication of the resolution. A significant difference between the approaches is the manner of determining the stress drop. In the solutions here the stress drop is one of the parameters adjusted to fit the observations. The slip distribution is then calculated for the inferred stress drop and geometry and used to determine the moment. In the kinematic models the slip magnitude and, possibly, distribution are chosen to fit the observations. The stress drop is then inferred from the moment, typically, by using the relation for a circular crack in an infinite body. As noted above, this relation is reasonably accurate, but significant loss in accuracy occurs if the slip zone is close to the free surface.

The additional information obtained by the present method is an estimate of the critical energy release rate (energy released per unit area advance of the slip zone). This estimate is obtained by assuming that the slip zone propagated according to the criterion that the energy release rate is equal to a critical value that reflects the resistance of the material. Although this criterion is simple, it is thought to be a good approximation when the actual inelastic processes associated with slip propagation occur in a zone near the slip zone edge that is small compared with other relevant length scales [*Rudnicki*, 1980; *Rice*, 1980, 1983; *Li*, 1987]. The slip zone stops advancing either because the available energy release decreases (perhaps due to a decrease in stress drop) or the slip zone has propagated into a region of higher critical energy release rate [*Husseini et al.*, 1975]. Thus the energy release rate inferred from the coseismic geodetic data is a lower bound on the critical energy release rate at the termination of rupture.

The critical energy release rates estimated for the three earthquakes considered here are $1.5 \times 10^6$ J/m$^2$ (Parkfield), $1.2 \times 10^6$ J/m$^2$ (Borah Peak), and $2 \times 10^8$ J/m$^2$ (Whittier Narrows). The value for Parkfield occurs at the top of the slip zone, and that for Borah Peak occurs at the ends of the surface trace of the slip zone. The Whittier Narrows event was deep enough that there was little variation around the edge. *Li* [1987] has tabulated values of the critical energy release rate inferred for crustal faulting (also see *Rudnicki* [1980]). These range from $10^0$ to $10^8$ J/m$^2$ with most of the values ranging from $10^5$ to $10^8$ J/m$^2$. The values inferred here are toward the upper end of this range, and that for the Whittier Narrows event is as large as any cited by *Li* [1987]. *Wong* [1982, 1986] has collected values of the critical energy release rate inferred from slip on sawcut laboratory specimens. These values are of the order of $10^4$ J/m$^2$ and hence about 2 orders of magnitude less than typical for crustal faults. *Martel and Pollard* [1989] have estimated values of critical shear fracture energy release rates ranging from $5 \times 10^2$ to $2 \times 10^4$ J/m$^2$, of the order of laboratory values, from field observations of slip along small faults in granite rock.

As indicated by this short summary, currently available estimates of values of the critical energy release rate for crustal faulting are not numerous and exhibit considerable variation. Additional estimates and knowledge of their variation through the crust would contribute to a better understanding of the initiation and arrest of earthquake ruptures.

## APPENDIX

The terms $K_{mn}$ in (7) relative to the crack surface coordinate system $y_i$ are given below:

$$K_{11} = \frac{\mu}{4\pi(\kappa+1)}\left\{\frac{2}{r_1^3}(\kappa-1) + \frac{3}{r_1^5}(3-\kappa)(y_1-\xi_1)^2 + \frac{2}{r_2^3}(\sin^2\alpha - \kappa + \kappa^2\cos^2\alpha) + \frac{3\bar{y}}{r_2^5}[-1-2\sin^2\alpha + \kappa(2\cos^2\alpha+1)] + \frac{12H}{r_2^5}(-5+7\cos^2\alpha + \kappa\sin^2\alpha) + \frac{120H}{r_2^7}[4H\sin^2\alpha + \bar{y}^2(3-4\cos^2\alpha)] - \frac{3360H^2\bar{y}^2\sin^2\alpha}{r_2^9} - 6\cos^2\alpha T_3\right\}$$

$$K_{12} = \frac{\mu}{4\pi(\kappa+1)}\left\{\frac{3}{r_1^5}(3-\kappa)(y_1-\xi_1)(y_2-\xi_2) + \frac{6\bar{y}\cos\alpha}{r_2^5}(h+y_2\cos\alpha) \cdot [-1+12\sin^2\alpha - \kappa(1+4\sin^2\alpha)] - \frac{3\bar{y}}{r_2^5}(y_2-\xi_2)[(1+4\sin^2\alpha - 2\sin^4\alpha) - \kappa(2\cos^2\alpha+1) - 2\kappa^2\sin^2\alpha\cos^2\alpha] + \frac{120H\bar{y}}{r_2^7}[2\cos\alpha(h+y_2\cos\alpha)(\kappa\sin^2\alpha + 7\cos\alpha - 6) + (y_2-\xi_2)(3-4\cos^2\alpha)] + \frac{3360H^2\sin^2\alpha\bar{y}}{r_2^9} \cdot [2\cos\alpha(h+y_2\cos\alpha) - (y_2-\xi_2)] - \frac{3}{2}\bar{y}\sin^2\alpha T_2\right\}$$

$$K_{13} = \frac{\mu\bar{y}\sin\alpha}{4\pi(\kappa+1)}\left\{\frac{24\cos^2\alpha}{r_2^5}(3-\kappa)(h+y_2\cos\alpha) - \frac{6\cos^3\alpha}{r_2^5}(1-\kappa^2)(y_2-\xi_2) + \frac{120H}{r_2^7}\cdot[(h+y_2\cos\alpha)(-1-7\cos 2\alpha+2\kappa\cos^2\alpha) - (y_2-\xi_2)(\kappa-1)\cos\alpha] - \frac{6720H^2\sin^2\alpha}{r_2^9}\cdot(h+y_2\cos\alpha) - 6\cos^3\alpha T_2\right\}$$

$$K_{22} = \frac{\mu}{4\pi(\kappa+1)}\left\{\frac{2}{r_1^3}(\kappa-1) + \frac{3}{r_1^5}(3-\kappa)(y_2-\xi_2)^2 + \frac{\cos 4\alpha}{r_2^3}(-7+\kappa) + \frac{48H}{r_2^5}(2+5\sin^2\alpha - 27\sin^2\alpha\cos^2\alpha + \kappa\sin^2\alpha\cos^2\alpha) + \frac{3\bar{y}^2}{r_2^5}[(3-22\sin^2\alpha\cos^2\alpha) - \kappa\cos 4\alpha - 2\kappa^2\sin^2\alpha\cos^2\alpha] + \frac{3\sin^2 2\alpha\sin^2\alpha}{2r_2^5}(\kappa^2-1)(y_2-\xi_2)^2 + \frac{60H}{r_2^7}[-8H\sin^2 2\alpha(9-16\cos^2\alpha) + \bar{y}^2(-2+7\sin^2 2\alpha - 4\sin^2\alpha - \kappa\sin^2 2\alpha)] + \frac{3360H\sin^2\alpha}{r_2^9}(4H\sin^2\alpha - \bar{y}^2\cos 2\alpha) + \frac{3}{2}\sin^2 2\alpha T_1\right\}$$

$$K_{23} = \frac{\mu\sin\alpha}{4\pi(\kappa+1)}\left\{\frac{8\cos^3\alpha}{r_2^3}(4-\kappa) - \frac{24H\cos 2\alpha\cos\alpha}{r_2^5}(10-\kappa) + \frac{6\bar{y}^2\cos^3\alpha}{r_2^5}(-7+4\kappa-\kappa^2) + \frac{24\cos^2\alpha}{r_2^5}(y_2-\xi_2)[2h+(y_2+\xi_2)\cos\alpha] + \frac{3\sin^2 2\alpha\cos\alpha}{2r_2^5}(y_2-\xi_2)^2(\kappa^2-1) + \frac{120H\cos\alpha}{r_2^7}[-12H\sin^2\alpha + \bar{y}^2\cos 2\alpha(4-\kappa)] + \frac{1680H^2\bar{y}^2\sin 2\alpha\sin\alpha}{r_2^9} - \frac{120H}{r_2^7}\cdot(y_2-\xi_2)\left(3\cos 2\alpha + \frac{28H\sin^2\alpha}{r_2^7}\right)\cdot[2h+(y_2+\xi_2)\cos\alpha] + 6\cos^3\alpha T_1\right\}$$

$$K_{33} = \frac{\mu}{4\pi(\kappa+1)}\left\{\frac{4}{r_1^3} - \frac{4}{r_2^3}(1-2\cos^4\alpha+2\kappa\cos^4\alpha) - \frac{12H}{r_2^5}[2(1+10\cos^2\alpha-14\cos^4\alpha) + \kappa\sin^2\alpha] + \frac{6\bar{y}^2\cos^4\alpha}{r_2^5}(-3+4\kappa-\kappa^2) + \frac{3\sin^2 2\alpha\cos^2\alpha}{2r_2^5}\cdot(\kappa^2-1)(y_2-\xi_2)^2 + \frac{240H\sin^2\alpha}{r_2^7}\cdot[4H(5\cos^2\alpha-2) + (\kappa-1)\bar{y}^2\cos^2\alpha] + \frac{13440H^3\sin^4\alpha}{r_2^9} + 6\cos^4\alpha T_1\right\}$$

where

$$\kappa = 3-4\nu$$

$$T_1 = (\kappa^2-1)\left[\frac{1}{r_2r_4^2} - \frac{2\sin^2\alpha}{r_2^2r_4^2}\left(\frac{2}{r_4}+\frac{1}{r_2}\right)(y_2-\xi_2)^2 + \frac{\sin^4\alpha}{r_2^3r_4^2}\left(\frac{1}{r_2^2}+\frac{2}{r_2r_4}+\frac{2}{r_4^2}\right)(y_2-\xi_2)^4\right]$$

$$T_2 = (\kappa^2-1)(y_2-\xi_2)\left[\frac{1}{r_2^2r_4^2}\left(\frac{1}{r_2}+\frac{2}{r_4}\right) - \frac{\sin^2\alpha}{r_2^3r_4^2}\left(\frac{1}{r_2^2}+\frac{2}{r_2r_4}+\frac{2}{r_4^2}\right)(y_2-\xi_2)^2\right]$$

$$T_3 = (\kappa^2-1)\left[\frac{1}{r_2r_4^2} - \frac{\bar{y}^2\sin^2\alpha}{r_2^3r_4^2}\left(\frac{1}{r_2^2}+\frac{2}{r_2r_4}+\frac{2}{r_4^2}\right)(y_2-\xi_2)^2\right]$$

$$\bar{y} = y_1-\xi_1$$

$$r_1^2 = (y_1-\xi_1)^2 + (y_2-\xi_2)^2$$

$$r_2^2 = \bar{y}^2 + (y_2-\xi_2)^2 + 4H$$

$$r_4 = r_2 + 2h + (y_2+\xi_2)\cos\alpha$$

$$H = h^2 + h(y_2+\xi_2)\cos\alpha + y_2\xi_2\cos^2\alpha$$

The reciprocal theorem requires that $K_{ij}(y, \xi) = K_{ji}(\xi, y)$, and this relation determines the remaining elements of $K_{ij}$.

The displacements in the elastic half-space are obtained by using (4), which can be written as follows:

$$u_i(\mathbf{x}) = \int_S \bar{K}_{in}(\mathbf{x}, \boldsymbol{\eta}) b_n(\boldsymbol{\eta})\, d\boldsymbol{\eta}$$

where

$$\bar{K}_{in}(\mathbf{x}, \boldsymbol{\eta}) = C_{jlmn} n_m \frac{\partial G_{ij}}{\partial \eta_l}(\mathbf{x}, \boldsymbol{\eta})$$

The terms $\bar{K}_{in}$ relative to the half-space coordinate system $x_i$ are listed below:

$$\bar{K}_{i1}(\mathbf{x}, \boldsymbol{\eta}) = \mu\left[-\sin\alpha\left(\frac{\partial G_{i1}}{\partial \eta_2} + \frac{\partial G_{i2}}{\partial \eta_1}\right) + \cos\alpha\left(\frac{\partial G_{i1}}{\partial \eta_3} + \frac{\partial G_{i3}}{\partial \eta_1}\right)\right]$$

$$\bar{K}_{i2}(\mathbf{x}, \boldsymbol{\eta}) = \mu\left[-\sin 2\alpha\left(\frac{\partial G_{i2}}{\partial \eta_2} - \frac{\partial G_{i3}}{\partial \eta_3}\right) + \cos 2\alpha\left(\frac{\partial G_{i3}}{\partial \eta_2} + \frac{\partial G_{i2}}{\partial \eta_3}\right)\right]$$

$$\bar{K}_{i3}(\mathbf{x}, \boldsymbol{\eta}) = \lambda \frac{\partial G_{ij}}{\partial \eta_j} + 2\mu\left[\sin^2\alpha \frac{\partial G_{i2}}{\partial \eta_2} + \cos^2\alpha \frac{\partial G_{i3}}{\partial \eta_3} - \sin\alpha\cos\alpha\left(\frac{\partial G_{i2}}{\partial \eta_3} + \frac{\partial G_{i3}}{\partial \eta_2}\right)\right]$$

The derivatives of the Green's function are as follows:

$$\frac{\partial G_{ij}}{\partial \eta_n} = \frac{1}{16\pi\mu(1-\nu)}\left\{-(3-4\nu)\frac{\delta_{ij}}{R_1^2}\frac{\partial R_1}{\partial \eta_n} - \frac{\delta_{ij}}{R_2^2}\frac{\partial R_2}{\partial \eta_n} - \left[\frac{1}{R_1^3} + \frac{(3-4\nu)}{R_2^3}\right] \cdot [\delta_{in}(x_j - \eta_j) + \delta_{jn}(x_i - \eta_i)] - 3(x_i - \eta_i)(x_j - \eta_j)\left[\frac{1}{R_1^4}\frac{\partial R_1}{\partial \eta_n} + \frac{(3-4\nu)}{R_2^4}\frac{\partial R_2}{\partial \eta_n}\right] + \frac{2x_2\delta_{2n}\delta_{ij}}{R_2^3} - \frac{6x_2\eta_2\delta_{ij}}{R_2^4}\frac{\partial R_2}{\partial \eta_n} + \frac{6x_2}{R_2^5}[\delta_{in}\eta_2(x_j - \eta_j) + \delta_{jn}\eta_2(x_i - \eta_i) - \delta_{2n}(x_i - \eta_i)(x_j - \eta_j)] + \frac{30x_2\eta_2}{R_2^6}\frac{\partial R_2}{\partial \eta_n} \cdot (x_i - \eta_i)(x_j - \eta_j) - 4(1-\nu)(1-2\nu)\frac{\delta_{ij}}{\bar{R}_2^2}\frac{\partial \bar{R}_2}{\partial \eta_n} + \frac{4}{R_2\bar{R}_2^2}(1-\nu)(1-2\nu)[\delta_{in}(x_j - \eta_j) + \delta_{jn}(x_i - \eta_i)] + 4(1-\nu)(1-2\nu)(x_i - \eta_i)(x_j - \eta_j) \cdot \left[\frac{1}{R_2\bar{R}_2^2}\frac{\partial R_2}{\partial \eta_n} + \frac{1}{R_2\bar{R}_2^3}\frac{\partial \bar{R}_2}{\partial \eta_n}\right]\right\} \quad i, j = 1, 3$$

$$\frac{\partial G_{2j}}{\partial \eta_n} = \frac{1}{16\pi\mu(1-\nu)}\left\{-\left[\frac{1}{R_1^3} + \frac{(3-4\nu)}{R_2^3}\right] \cdot [\delta_{2n}(x_j - \eta_j) + \delta_{jn}(x_2 - \eta_2)] - \frac{3}{R_1^4}\frac{\partial R_1}{\partial \eta_n}(x_2 - \eta_2)(x_j - \eta_j) - \frac{3(3-4\nu)}{R_2^4}\frac{\partial R_2}{\partial \eta_n}(x_2 - \eta_2)(x_j - \eta_j) + \frac{6x_2}{R_2^5}[\delta_{jn}\eta_2(x_2 + \eta_2) - \delta_{2n}(x_j - \eta_j) \cdot (x_2 + \eta_2) - \delta_{2n}\eta_2(x_j - \eta_j)] + \frac{30x_2\eta_2}{R_2^6}\frac{\partial R_2}{\partial \eta_n}(x_2 + \eta_2)(x_j - \eta_j) - \frac{4\delta_{jn}}{R_2\bar{R}_2}(1-\nu)(1-2\nu) - 4(1-\nu) \cdot (1-2\nu)(x_j - \eta_j)\left(\frac{1}{R_2^2\bar{R}_2}\frac{\partial R_2}{\partial \eta_n} + \frac{1}{R_2\bar{R}_2^2}\frac{\partial \bar{R}_2}{\partial \eta_n}\right)\right\} \quad j = 1, 3$$

$$\frac{\partial G_{i2}}{\partial \eta_n} = \frac{1}{16\pi\mu(1-\nu)}\left\{-\left(\frac{1}{R_1^3} + \frac{(3-4\nu)}{R_2^3}\right) \cdot [\delta_{2n}(x_i - \eta_i) + \delta_{in}(x_2 - \eta_2)] - \frac{3}{R_1^4}\frac{\partial R_1}{\partial \eta_n}(x_2 - \eta_2)(x_i - \eta_i) - \frac{3(3-4\nu)}{R_2^4}\frac{\partial R_2}{\partial \eta_n}(x_2 - \eta_2)(x_i - \eta_i) + \frac{6x_2}{R_2^5}[\delta_{2n}(x_2 + \eta_2)(x_i - \eta_i) + \delta_{2n}\eta_2(x_i - \eta_i) - \delta_{in}\eta_2(x_2 + \eta_2)] - \frac{30x_2\eta_2}{R_2^6}\frac{\partial R_2}{\partial \eta_n}(x_2 + \eta_2)(x_i - \eta_i) + \frac{4\delta_{in}}{R_2\bar{R}_2}(1-\nu)(1-2\nu) + 4(1-\nu)(1-2\nu)(x_i - \eta_i) \cdot \left(\frac{1}{R_2^2\bar{R}_2}\frac{\partial R_2}{\partial \eta_n} + \frac{1}{R_2\bar{R}_2^2}\frac{\partial \bar{R}_2}{\partial \eta_n}\right)\right\} \quad i = 1, 3$$

$$\frac{\partial G_{22}}{\partial \eta_n} = \frac{1}{16\pi\mu(1-\nu)} \left\{ -\frac{(3-4\nu)}{R_1^2}\frac{\partial R_1}{\partial \eta_n} - \frac{2\delta_{2n}}{R_1^3}(x_2-\eta_2) - \frac{3}{R_1^4}\frac{\partial R_1}{\partial \eta_n}(x_2-\eta_2) - \frac{1}{R_2^2}\frac{\partial R_2}{\partial \eta_n}[8(1-\nu)^2-(3-4\nu)] + \frac{2\delta_{2n}}{R_2^3} \cdot [(3-4\nu)(x_2+\eta_2)-x_2] - \frac{3}{R_2^4}\frac{\partial R_2}{\partial \eta_n} \cdot [(3-4\nu)(x_2+\eta_2)^2 - 2x_2\eta_2] + \frac{6\delta_{2n}x_2}{R_2^5}(x_2+\eta_2)^2 + \frac{12\delta_{2n}x_2\eta_2}{R_2^5}(x_2+\eta_2) - \frac{30x_2\eta_2}{R_2^6}\frac{\partial R_2}{\partial \eta_n}(x_2+\eta_2)^2 \right\}$$

where

$$R_1 = [(x_1-\eta_1)^2 + (x_2-\eta_2)^2 + (x_3-\eta_3)^2]^{1/2}$$

$$R_2 = [(x_1-\eta_1)^2 + (x_2+\eta_2) + (x_3-\eta_3)^2]^{1/2}$$

$$\bar{R}_2 = R_2 + x_2 + \eta_2$$

*Acknowledgments.* This work has been supported jointly by the National Science Foundation and the U.S. Geological Survey through NSF grant EAR-8707392. Ross Stein provided the data for the Borah Peak and Whittier Narrows earthquakes. Paul Segall provided the data for the Parkfield earthquake. It is a pleasure to acknowledge their help. Thoughtful comments by reviewers Ruth Harris and Stephen Martel and by Associate Editor Jack Boatwright substantially improved the manuscript. In addition, we are grateful to Alan Rubin for pointing out an error in the sign of the normal relative displacement caused by slip.

## REFERENCES

Aki, K., Origin of the seismic gap: What initiates and stops a rupture propagation along a plate boundary?, in Proceedings of Conference VI, Methodology for Identifying Seismic Gaps and Soon-to-Break Gaps, 1978, *U.S. Geol. Surv. Open File Rep., 78-943*, 3–46, 1978.

Archuleta, R. J., and S. M. Day, Dynamic rupture in a layered medium: The 1966 Parkfield earthquake, *Bull. Seismol. Soc. Am., 70*, 671–689, 1980.

Barrientos, S. E., R. S. Stein, and S. N. Ward, Comparison of the 1959 Hebgen Lake, Montana and the 1983 Borah Peak, Idaho, earthquakes from geodetic observations, *Bull. Seismol. Soc. Am., 77*, 784–808, 1987.

Chinnery, M. A., The deformation of the ground around surface faults, *Bull. Seismol. Soc. Am., 51*, 355–372, 1961.

Davis, T. L., J. Namson, and R. F. Yerkes, A cross section of Los Angeles basin: Seismically active fold and thrust belt, the Whittier Narrows earthquake and earthquake hazard along the northern edge of the Los Angeles basin, *J. Geophys. Res., 94*, 9644–9664, 1989.

Dmowska, R., and B. V. Kostrov, A shearing crack in a semi-space under plane strain conditions, *Arch. Mech., 25*, 421–440, 1973.

Dmowska, R., and J. R. Rice, Fracture theory and its seismological applications, in *Continuum Theories in Solid Earth Physics*, edited by R. Teisseyre, pp. 187–255, Polish Scientific, Warsaw, 1986.

Doser, D. I., and R. B. Smith, Source parameters of the October 28, 1983 Borah Peak, Idaho, earthquake from body wave analysis, *Bull. Seismol. Soc. Am., 75*, 1041–1051, 1985.

Eaton, J. P., M. E. O'Neill, and J. M. Murdock, Aftershocks of the 1966 Parkfield-Cholame, California earthquake: A detailed study, *Bull. Seismol. Soc. Am., 60*, 1151–1197, 1970.

Eshelby, J. D., The determination of the elastic field of an ellipsoidal inclusion, and related problems, *Proc. R. Soc. London, Ser. A, 241*, 276–396, 1957.

Husseini, M. I., D. B. Jovanovich, M. J. Randall, and L. B. Freund, The fracture energy of earthquakes, *Geophys. J. R. Astron. Soc., 43*, 367–385, 1975.

King, N. E., P. Segall, and W. Prescott, Geodetic measurements near Parkfield, California, 1959–1984, *J. Geophys. Res., 92*, 2474–2766, 1987.

Kostrov, B. V., and S. Das, Evaluation of stress and displacement fields due to an elliptical plane shear crack, *Geophys. J. R. Astron. Soc., 78*, 19–33, 1984.

Lee, J. C., and L. M. Keer, Study of a three-dimensional crack terminating at an interface, *J. Appl. Mech., 108*, 311–316, 1986.

Lee, J. C., T. N. Farris, and L. M. Keer, Stress intensity factors for cracks of arbitrary shape near an interfacial boundary, *Eng. Fract. Mech., 27*, 27–41, 1987.

Li, V., Mechanics of shear rupture applied to earthquake zones, in *Rock Fracture Mechanics and Geophysics*, edited by B. Atkinson, Academic, pp. 351–428, Academic, San Diego, Calif., 1987.

Lin, J., and R. S. Stein, Coseismic folding, earthquake recurrence, and the 1987 source mechanism at Whittier Narrows, Los Angeles basin, California, *J. Geophys. Res., 94*, 9614–9632, 1989.

Mansinha, L., and D. E. Smylie, The displacement fields on inclined faults, *Bull. Seismol. Soc. Am., 61*, 1433–1440, 1971.

Martel, S. J., and D. D. Pollard, Mechanics of slip and fracture along small faults and simple strike-slip fault zones in granite rock, *J. Geophys. Res., 94*, 9417–9428, 1989.

Mindlin, R. D., Force at a point in the interior of a semi-infinite solid, *Physics, 7*, 195–202, 1936.

Mindlin, R. D., Force at a point in the interior of a semi-infinite solid, *Proc. Midwest. Conf. Solid Mech., 1st*, 56–59, 1955.

Mindlin, R. D., and D. H. Cheng, Nuclei of strain in the semi-infinite solid, *J. Appl. Phys., 21*, 926–933, 1950.

Murakami, Y. (Ed.), *Stress Intensity Factors Handbook*, vol. 2, Pergamon, New York, 1987.

Murakami, Y., and S. Nemat-Nasser, Growth and stability of interacting surface flaws of arbitrary shape, *Eng. Fract. Mech., 17*, 193–210, 1983.

Rice, J. R., Mathematical analysis in the mechanics of fracture, in *Fracture: An Advanced Treatise*, vol. 2, edited by H. Liebowitz, pp. 191–311, Academic, San Diego, Calif., 1968.

Rice, J. R., The mechanics of earthquake rupture, in Physics of the Earth's Interior, edited by A. M. Dziewonski and E. Boschi, *Proc. Int. School Phys. Enrico Fermi, 78*, 555–649, 1980.

Rice, J. R., Constitutive relations for fault slip and earthquake instabilities, *Pure Appl. Geophys., 121*, 443–475, 1983.

Richins, W. D., R. B. Smith, C. J. Lanser, J. E. Zollweg, J. T. King, and J. C. Pechmann, The 1983 Borah Peak, Idaho, earthquake: Relationship of aftershocks to mainshock, surface faulting, and regional tectonics, in Workshop XXVIII on the Borah Peak Earthquake, *U.S. Geol. Surv., Open File Rep. 85-290*, 285–310, 1985.

Rudnicki, J. W., Fracture mechanics applied to the earth's crust, *Annu. Rev. Earth Planet. Sci., 8*, 489–525, 1980.

Segall, P., and R. Harris, Earthquake deformation cycle on the San Andreas fault near Parkfield, California, *J. Geophys. Res., 92*, 10,511–10,525, 1987.

Smith, S. W., and M. Wyss, Displacement on the San Andreas fault subsequent to the 1966 Parkfield earthquake, *Bull. Seismol. Soc. Am., 58*, 1955–1973, 1968.

Stein, R. S., and S. E. Barrientos, High-angle normal faulting in the intermountain seismic belt: Geodetic investigation of the 1983 Borah Peak, Idaho earthquakes, *J. Geophys. Res., 90*, 11,355–11,366, 1985.

Steketee, J. A., Some geophysical applications of the elasticity theory of dislocations, *Can. J. Phys., 36*, 1168–1198, 1958.

Stuart, W. D., R. J. Archuleta, and A. G. Lindh, Forecast model for moderate earthquakes near Parkfield, California, *J. Geophys. Res., 90*, 592–604, 1985.

Tsai, Y.-B., and K. Aki, Simultaneous determination of the seismic

moment and attenuation of seismic surface waves, *Bull. Seismol. Soc. Am.*, *59*, 275–287, 1969.
Wong, T.-F., Shear fracture energy of Westerly granite from post-failure behavior, *J. Geophys. Res.*, *87*, 990–1000, 1982.
Wong, T.-F., On the normal stress dependence of the shear fracture energy, in Earthquake Source Mechanics *Geophys. Monogr. Ser.*, vol. 37, edited by S. Das, J. Boatwright, and C. H. Scholz, pp. 1–11, AGU, Washington, D. C., 1986.

L. M. Keer, C. H. Kuo, J. W. Rudnicki, and M. Wu, Department of Civil Engineering, Northwestern University, Evanston, IL, 60208-3109.

(Received August 2, 1990;
revised February 27, 1991;
accepted April 8, 1991.)